SPH-FV coupling algorithm for solving multi-scale three-dimensional free-surface flows

A. Di Mascio [a], S. Marrone [b,*], A. Colagrossi [b], L. Chiron [c], D. Le Touzé [d]

[a] *DIIIE, Università degi Studi dell'Aquila, Monteluco di Roio (AQ), Italy*

[b] *CNR-INM, Institute of Marine Engineering, Rome, Italy*

[c] *NEXTFLOW Software, Nantes, France*

[d] *Ecole Centrale Nantes, LHEEA Lab. (UMR CNRS), Nantes, France*

Abstract

In two previous papers we presented an algorithm for coupling the Finite Volume (FV) method for the solution of 2D Navier-Stokes equations dicretized on block structured Eulerian grids with the weakly-compressible Lagrangian Smoothed Particle Hydrodynamcs (SPH) method. This coupling procedure exploits the SPH method to discretize flow regions close to free-surfaces and the Finite Volume approach to resolve both the bulk flow and the wall regions, where grid stretching can be favourably used. The information exchange between the two numerical schemes is established through overlapping zones. In the present paper this coupling paradigm is extended to a 3D framework. To this purpose, the extension of the algorithms for particle creation/deletion on the interfaces are described and issues related to free-surface intersection with each sub-domain boundary are addressed. Moreover, a new coupling procedure that simplifies the algorithm is proposed and tested. Effectiveness and accuracy achieved by the coupled solver are tested on challenging problems involving large free surface deformations and vorticity generation like the 3D flow past a cylinder below a free surface, the breaking wave generated by a ship bow in forward motion and the impact of a flat plate on the water surface.

Key words:
Smoothed Particle Hydrodynamics, Finite Volume Method, Domain decomposition, Coupling algorithms

* Corresponding author:
Email address: salvatore.marrone@cnr.it (S. Marrone).

1 Introduction

The simulation of free surface flows close to rigid boundaries, for both basic research and design purposes, requires numerical algorithms able to capture both the complex free surface evolution, possibly with relevant breaking and fragmentation, and the details of vorticity production in thin boundary layers on rigid walls and its evolution in the bulk flow. With this kind of problems the main difficulties for reliable simulations stem from both the topological variation of the computational domain due to the free surface evolution, more easily handled by Lagrangian approaches, and from the need for a proper resolution of the vorticity field in the boundary layer and wakes where space discretization is more easily controlled with Eulerian grids.

In order to exploit the best of the two approaches, in [26] an algorithm that couples the Smoothed Particle Hydrodynamics (SPH) approach with a Finite Volume (FV) scheme was developed and implemented. The results proved that for certain kind of flows (e.g. wave propagation and breaking in deep water) the algorithm is both very accurate and efficient.

Of course, the idea of domain decomposition is by no means new and has been largely exploited in fluid dynamics. A classical review of coupling methods between Eulerian solvers can be found in [20], whereas a review of domain decomposition with particle methods can be found in [16] and, more recently, in [40]. Coupling methods between mesh–based and particle approaches were proposed, besides [26], in [31] where an incompressible SPH model is coupled with an incompressible FV approach with surface fitting. Other examples can be found in [4, 19] where both particle methods and FV solvers are exploited to improve the quality of the solution.

The algorithm proposed in [26] was improved to handle both net mass transfer and free surface passage through the coupling boundary in [5]. In the present paper, the algorithm is extended to a 3D environment; to this purpose, the interface boundary on the SPH side is supplemented with a procedure to add and remove particles, so that open-boundary conditions can be included to limit the region where the SPH solution is performed. Similarly to what proposed in [2] the seeding/de–seeding region is controlled by the solution exchanged with the adjacent FV solution, and particle production is carried out with particular attention to global mass conservation.

At the same time, in the overlapping zone on the FV side particle trajectories are exploited to correct the free surface position, in a way that resembles the Particle/Level Set algorithms (see, e.g. [13]), the information obtained from the SPH solution being used to guarantee consistency between the two solutions also in case of violent free–surface motion.

The numerical results reported in the present paper for three dimensional problems show that, by properly coupling the two approaches, it is possible to obtain an algorithm that retains the best from each discretization technique, even when dealing with flows characterized by different length and time scales. In particular, we aim to exploit the ability of Lagrangian particle methods to simulate free surface flows, possibly with front fragmentation, without mass or momentum losses; at the same time, we retain the ability of mesh–based approaches (chimera-type approaches in the specific) to simulate the flow around body with complex frontiers and to control grid clustering in boundary layers and wakes.

In fact, the SPH approximation renders the simulation of the fragmented front region far more accurate than what can be obtained by the Finite Volume–Level Set simulation with a comparable number of cells in the same region; nevertheless, SPH would also demand a large number of particles to discretize the regions where the flow is smooth and characterized by length scales much larger than the kernel support. The behaviour of the FV approach is complementary: it is very easy to control grid stretching and/or clustering in prefixed flow regions (e.g. boundary layers), but it is very CPU and memory demanding when there is the need to capture the fine details of the breaking front, because the whole region where the free surface evolves should be covered with an extremely refined grid.

On the basis of the above considerations, the flow domain is split in two regions and the SPH approximation is applied only where the free-surface deformations are relevant, whereas we take advantage of the Finite Volume solution elsewhere. In order to allow information exchange, at the boundary of the SPH domain the solution from the underlying FV grid is transferred by trilinear interpolation of the values at the cell centres on a slice of SPH particles. Similarly, the solution on the FV grid is obtained by an SPH–type interpolation (Shepard interpolation) on two slices of ghost cells.

In order to avoid discontinuities on the SPH field, the FV solution is blended with the one from SPH over an overlapping zone, hereinafter called the “blending region”. A further slice of particles is added after this transition zone where particles are purely forced through the FV solution.

The way in which the particles are created and removed at the boundary of the interaction zone is the natural extension to 3D of the algorithm presented in [5]: the generation of particles is performed by computing the net mass flow through each sub–portion of the boundary surface (rectangles, in the present case) and by injecting a particle when the cumulative mass flow equate the prefixed particle mass. Conversely, a particle close to the interface is removed from the SPH set when the computed outflow mass is equal to the particle mass.

In the present 3D implementation we also tested an alternative way to couple the two solvers, which will be more convenient when dealing with moving bodies.

Specifically, the region covered by the SPH domain is not removed from the FV domain that instead covers the whole flow domain. In this case the solution on the Eulerian grid is computed by adding a forcing term in the region overlapped by the SPH solution. This forcing term is identical to what done in the "Chimera–type" approach, already used to couple the solution between overlapping block–structured meshes (see, for instance, [10, 30]). This way of coupling allows to greatly simplify the grid set-up for the Finite-Volume (there is no need to remove portion of the grid to conform the SPH domain) and, moreover, makes the simulation of problems with moving SPH domains easier.

Of course, the global algorithm for 3D problems is somewhat more involved than for 2D problems, particularly for particle handling on the interfaces and donor search when dealing with highly stretched grids. This aspects will be discussed in details in the following sections. In the next sections the adopted mathematical models and numerical schemes are presented.

2 Mathematical models

For both (Lagrangian and Eulerian) approaches, the weakly compressible flow model is adopted, i.e. the fluid is supposed to be barotropic and therefore the fluid density ρ depends only on the pressure p; in addition, in the hypothesis of weak compressibility

$$\frac{d\rho}{dp} = \frac{1}{c^2},$$

where c (the sound speed) is supposed to be constant and large with respect to the typical fluid velocity U; generally, this condition is fulfilled by imposing the flow Mach number $\mathrm{Ma} = U/c \leq 0.1$.

2.1 Lagrangian formulation

With the above assumptions, mass and momentum equations, i.e.

$$\begin{cases} \dfrac{D\rho}{Dt} + \rho\nabla\cdot\mathbf{u} = 0 \\ \rho\dfrac{D\mathbf{u}}{Dt} + \nabla p + \rho g\mathbf{k} = \nabla\cdot\mathbb{T} \\ \dfrac{D\mathbf{x}}{Dt} = \mathbf{u} \end{cases} \tag{1}$$

can be solved independently from the energy equation. In equations (1), $D()/Dt$ is the material derivative, $\mathbf{x}$ is the position vector of the material point, $\mathbf{u} = \mathbf{u}(t, \mathbf{x})$ is

the velocity vector, g the acceleration of gravity, $\mathbf{k}$ the upward unit vector, $\mathbb{T}$ the stress tensor, given by

$$\mathbb{T} = \mu \left[\nabla \mathbf{u} + \nabla \mathbf{u}^T \right] \tag{2}$$

being μ the dynamic viscosity of the fluid.

2.2 Eulerian formulation

In Eulerian formulation, the Navier–Stokes equations are written in full conservation form as

$$\begin{cases} \dfrac{\partial \rho}{\partial t} + \nabla \cdot (\rho \mathbf{u}) = 0 \\ \dfrac{\partial \rho \mathbf{u}}{\partial t} + \nabla \cdot (\rho \mathbf{u} \otimes \mathbf{u}) + \nabla p + \rho g \mathbf{k} = \nabla \cdot \mathbb{T} \end{cases} \tag{3}$$

3 Numerical methods

3.1 Finite volume scheme

The discretization of Navier-Stokes equations in their Eulerian formulation is made by means of a Finite Volume (FV) scheme, implemented on a multi–block structured grid with partial overlapping ([10, 30]); with this approach, the computational domain is split into sub-domains

$$D^l, \qquad l = 1, \ldots, L$$

not necessarily disjoint. A curvilinear coordinate system (ξ, η, ζ) is considered on each block, discretized by a structured grid with hexahedral cells

$$D^l_{i,j,k} \qquad i = 1, \ldots, N_i \quad j = 1, \ldots, N_j \quad k = 1, \ldots, N_k$$

where the indexes i, j, k runs along each coordinate direction.

The equations are then integrated over each sub–domain; the time derivative is approximated by a second order fully implicitly three–point backward formula.

The resulting discrete system reads, at time $t = t^n$,

$$\begin{aligned} V_{i,j,k}\frac{3\rho\mathbf{u}^n_{i,j,k} - 4\rho\mathbf{u}^{n-1}_{i,j,k} + \rho\mathbf{u}^{n-2}_{i,j,k}}{2\Delta t} &+ \mathbf{F}^n_{i+1/2,j,k} - \mathbf{F}^n_{i-1/2,j,k} \\ &+ \mathbf{F}^n_{i,j+1/2,k} - \mathbf{F}^n_{i,j-1/2,k} \\ &+ \mathbf{F}^n_{i,j,k+1/2} - \mathbf{F}^n_{i,j,k-1/2} \\ &+ g\mathbf{k}\,\rho_{i,j,k}\,V_{i,j,k} = 0 \end{aligned} \tag{4}$$

where $\mathbf{F} = [\rho(\mathbf{u}\cdot\mathbf{n})\mathbf{u} + p\mathbf{n} - \mathbb{T}\cdot\mathbf{n}]\,S^\xi$ is, e.g., the flux integral on the cell face normal to the curvilinear coordinate ξ whose measure is S^ξ and $\mathbf{F}^n_{i+1/2,j,k}$ is its approximation computed at time t^n on the face between cells i, j, k and $i+1, j, k$. $V_{i,j,k}$ is the cell volume. Analogously, mass conservation reads

$$\begin{aligned} & V_{i,j,k}\frac{3\rho^n_{i,j,k} - 4\rho^{n-1}_{i,j,k} + \rho^{n-2}_{i,j,k}}{2\Delta t} \\ & +\rho U^\xi|^n_{i+1/2,j,k} - \rho U^\xi|^n_{i-1/2,j,k} \\ & +\rho U^\eta|^n_{i,j+1/2,k} - \rho U^\eta|^n_{i,j-1/2,k} \\ & +\rho U^\zeta|^n_{i,j,k+1/2} - \rho U^\zeta|^n_{i,j,k-1/2} = 0 \end{aligned} \tag{5}$$

where, for instance, $U^\xi = \mathbf{u}\cdot\mathbf{n}\,S^\xi$ is the volume flux normal to the face S^ξ.

The pressure p is computed from the linear state equation

$$\rho = \rho_0 + \frac{p - p_0}{c^2}$$

ρ_0 and p_0 being the reference density and pressure values at the free surface.

The resulting system (4-5) being fully coupled and non–linear, it is solved by a dual time step approach, in which the original system is substituted by

$$\begin{aligned} V\frac{\partial\mathbf{u}}{\partial\tau} + \frac{1}{\rho}\ [LHS\ of\ eq.\ 4] = 0 \\ V\frac{\partial p}{\partial\tau} + \beta\ [LHS\ of\ eq.\ 5] = 0 \end{aligned} \tag{6}$$

where $\sqrt{\beta}$ is a pseudo–sound speed. System (6) is then discretized by computing pressure and volume flux term by means of a high order Godunov–type scheme, as described in [12]. Note than the system (6) returns to the incompressible model when $c \to \infty$. Moreover, the leading order dissipation terms in the truncation error do not depend on the actual speed of sound but on the pseudo–sound speed and can be therefore controlled independently from the Mach number, so that the excessive numerical dissipation of standard Godunov–type approaches, observed for vanishing Mach number, can be easily circumvented.

When dealing with free surface flows, the above numerical scheme is coupled with a level–set approach like in [9]. The position of the free boundary is identified by the zero level of a level–set function $\phi(\mathbf{x}, t)$, whose modulus is equal to the distance from the moving frontier; the sign of the function is positive above the water domain and negative below. This function evolves with the solution as a material property of the fluid, i.e. its material derivative is set to zero:

$$\frac{D\phi}{Dt} = \frac{\partial \phi}{\partial t} + \mathbf{u} \cdot \nabla \phi = 0. \tag{7}$$

Therefore, the zero level of ϕ, if initially coincident with the free surface, remains on the boundary. The FV algorithm is locally modified in the cells cut by the free surface, in order to enforce the free surface dynamic boundary conditions. Moreover, the level–set function is reinitialized as a signed distance function at each time step, in order to limit the mass defect/gain associated to the non conservative form of the algorithm. The reader is referred to [9] and to the bibliography reported therein for details.

3.2 Smoothed Particle Hydrodynamics scheme

The adopted SPH model is a Riemann-based SPH scheme without mass fluxes [36], resulting in the following discrete equations :

$$\frac{d}{dt}(\mathbf{x}_i) = \mathbf{u}_{0i}, \tag{8}$$

$$\frac{d}{dt}(V_i) = 2V_i \sum_{j \in \mathcal{P}} V_j \left(\mathbf{u}_E - \mathbf{u}_i\right) \cdot \nabla_i W_{ij}, \tag{9}$$

$$\frac{d}{dt}(V_i \rho_i) = 0, \tag{10}$$

$$\frac{d}{dt}(V_i \rho_i \mathbf{u}_i) = V_i \rho_i \boldsymbol{g} - V_i \sum_{j \in \mathcal{P}} V_j 2 P_E \nabla_i W_{ij} + \mathbf{F}_i^v, \tag{11}$$

where V_i is the volume of the i-th particle, $W_{ij} = W(\boldsymbol{x}_i - \boldsymbol{x}_j)$ is the kernel function and $\mathbf{F}_i^v$ is the viscous force acting on the particle i and discretized following the Monaghan and Gingold formulation [27]; u_E and P_E are the solutions of the Riemann problem formed by the left (i) and right (j) states Several Riemann solvers can be found in the literature [28, 35, 39]. Here, the linearized Riemann solver as firstly proposed in SPH by [36] is chosen:

$$\begin{cases} \mathbf{u}_E = \dfrac{c(\rho_i \mathbf{u}_i + \rho_j \mathbf{u}_j) \cdot \mathbf{x}_{ij} + P_i - P_j}{c(\rho_i + \rho_j)} \mathbf{x}_{ij} \\ P_E = \dfrac{\rho_j P_i + \rho_i P_j + c\, \rho_i \rho_j \left(\mathbf{u}_i - \mathbf{u}_j\right) \cdot \mathbf{x}_{ij}}{\rho_i + \rho_j} \end{cases} \tag{12}$$

where $\mathbf{x}_{ij} = \frac{\mathbf{x}_j - \mathbf{x}_i}{\|\mathbf{x}_j - \mathbf{x}_i\|}$ and ρ_i,$\mathbf{u}_i$ and P_i are, respectively, the density, velocity and pressure of the i-th particle. The system is closed by a linear state equation as in the FV scheme:

$$P = c^2(\rho - \rho_0) + P_0$$

in which $P_0 = 0$. A particle-shifting technique as in [18] is applied by defining:

$$\mathbf{u}_{0i} = \mathbf{u}_i + \boldsymbol{\delta}_{ui} \qquad \text{with } \|\boldsymbol{\delta}_{ui}\| \ll \|\mathbf{u}_i\|, \tag{13}$$

where $\boldsymbol{\delta}_{ui}$ corresponds to a small velocity perturbation based on $U^{char} = c\text{Ma}$ (see [34] for more details):

$$\boldsymbol{\delta}_{ui} = \begin{cases} -U^{char}\,\hat{\boldsymbol{n}}_i & \text{if} \quad U^{char}\,\|\hat{\boldsymbol{n}}_i\| < 0.25\,\|\mathbf{u}_i\| \\ \\ -0.25\,\|\boldsymbol{u_i}\|\dfrac{\hat{\boldsymbol{n}}_i}{\|\hat{\boldsymbol{n}}_i\|} & \text{otherwise,} \end{cases} \tag{14}$$

$\hat{\boldsymbol{n}}_i$ is a vector pointing to the direction where voids appear in the particle distribution:

$$\hat{\boldsymbol{n}}_i = \sum_{j \in \mathcal{P}} V_0 \nabla_i W_{ij} R_i \tag{15}$$

where R is the kernel radius and $V_0 = \Delta x^D$, Δx being the mean particle spacing and D the dimension of the considered problem. Note that the method proposed here differs from [34] as the Riemann-SPH scheme is not written in an ALE formalism and mass fluxes are null. A MUSCL (Monotone Upstream Scheme for Conservation Laws) procedure is used to increase the order of this TVD scheme [41].

The kernel function W_{ij} used in this work is a C^2 Wendland kernel. In the present study where only 3D simulations are addressed, a kernel radius $R = 2.7\Delta x$ has been chosen, corresponding to about 80 interacting neighbors. The time step must respect a CFL (Courant-Friedrich-Lewy) condition which depends on the sound speed c for the hyperbolic part and on ν for the elliptic part of the Navier-Stokes equations:

$$\Delta t = \min\left(CFL_a \frac{R}{c}, CFL_\nu \frac{R^2}{\nu}\right) \tag{16}$$

where CFL_a is the Courant number, taken as $CFL_a = 0.375$, CFL_ν is the diffusion Courant number $CFL_\nu = 0.12$ and ν is the kinematic viscosity. The SPH scheme is advanced in time through a fourth-order Runge-Kutta scheme.

4 Coupling Algorithm

The proposed algorithm aims at exploiting the different behaviour of the two algorithms when dealing with problem characterized by different length scales.

In particular:

- the Smoothed Particle Hydrodynamics approach is very efficient when dealing with free surface flows, because its Lagrangian formulation is naturally convenient to track a fragmented free surface, even with relatively few particles. The same task, on the other side, is not so efficiently accomplished by Eulerian algorithms, like the Finite Volume method, for several reasons: first of all, some additional logic is required to find the position of the free surface with respect to the grid; moreover the integration requires proper local adaptation to enforce the free surface boundary conditions, as Level Set and Volume-of-Fluid approaches. Secondly, Eulerian approaches are inefficient because the grid used for the simulation must cover the entire region spanned by the free surface motion.
- Finite Volume approaches are very convenient to simulate high Reynolds number flows because they can make use of, for instance, block–structured mesh; by means of this kind of discretization it is very easy to control grid stretching in the boundary layers and grid refinement in the wake region. At the same time, it is easy to coarsen the mesh where the solution is smooth in order to improve the global efficiency. Local resolution, on the other side, is not easily controlled with SPH algorithms, for several reasons: the first is that the discrete particles follows the fluid particles trajectories, and consequently they tend to move away from rigid walls. This Lagrangian motion causes a depletion of particles in boundary layers, with related loss of accuracy. The second reason is that the SPH algorithm requires a particle distribution as homogeneous and isotropic as possible, in order to control dicretization error; consequently, particle clustering and depletion is an all but trivial task.

The details of the approach are described in what follows.

4.1 Spatial coupling

On the basis of the above considerations, the spatial domain is subdivided in order to retain the SPH solution in a limited region where free-surface deformations are more relevant and take advantage of the Finite Volume solution elsewhere.

Differently from what done in [5], we investigated two ways to handle the FV domain: in the first, the approach is the extension to 3D of the previous algorithm (referred to as *Coupling I* in the following), i.e. the FV domain is the complement to the inner SPH domain (top of figure 1); in the second, instead, the region overlapped by the SPH particles is not removed from the FV domain which covers the whole domain (*Coupling II*, bottom of figure 1). With this second approach, the algorithm can be greatly simplified and, in perspective, can be more easily extended to moving grid problems.

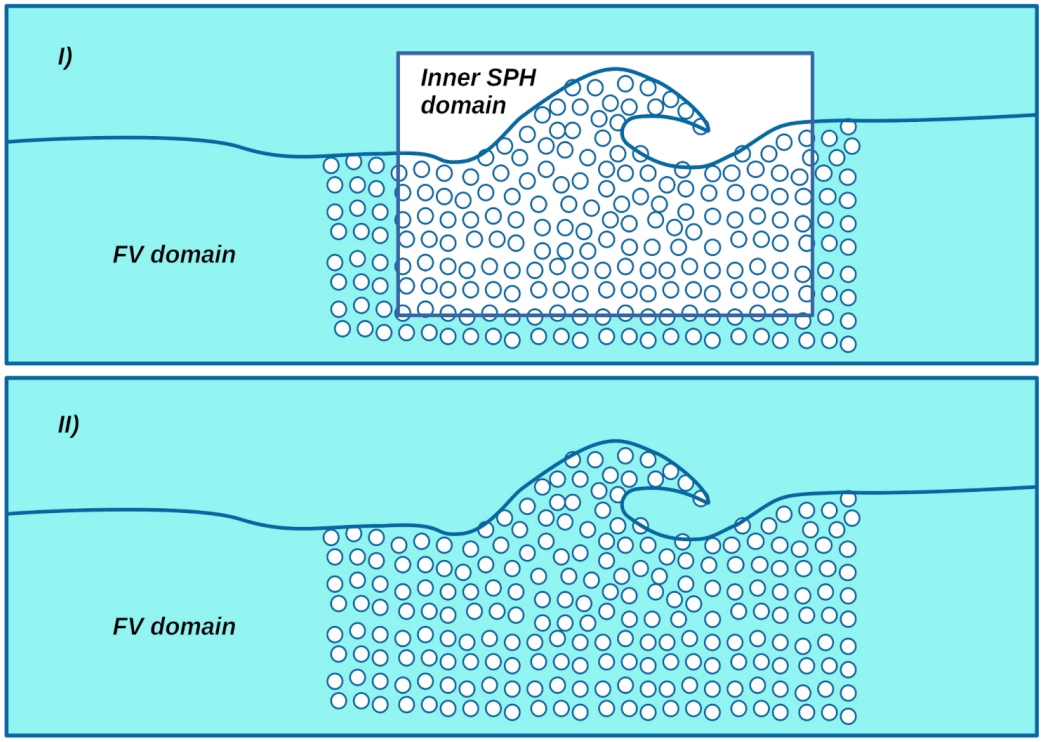

Fig. 1. Sketch of the two coupling strategies adopted: *Coupling I* (top plot) in which the SPH (white circles) and the FV (cyan region) domains are complementary and only a partial overlapping is performed; *Coupling II* (bottom plot) in which the FV domain covers the entire numerical domain and the SPH domain overlaps it only in the region of interest.

4.1.1 SPH domain

As already said, only the region around the wave breaking front is solved by the SPH approach. The way in which information is transferred from the FV solver to SPH one is depicted in figure 2.

In particular, the SPH domain consists of three separate regions:

(1) in the inner one (blue in figure 2) the solution is computed as in the standard SPH algorithm.
(2) In the intermediate region (green in figure 2), the velocity and pressure fields computed from the SPH solution are blended with the underlying FV solution with a weight that depends on the distance from the blending domain boundaries; in details, if d_e is the distance from the outermost boundary of the blending region and d_i the distance from the innermost one, the actual solution $(p, \mathbf{u})$ for the SPH solver is computed by blending the solution computed with the pure SPH algorithm $(p_{SPH}, \mathbf{u}_{SPH})$ with the one from the FV region $(p_{FV}, \mathbf{u}_{FV})$, as in the following formulas:

$$p = p_{FV}\frac{d_i}{d_e + d_i} + p_{SPH}\frac{d_e}{d_e + d_i}; \qquad \mathbf{u} = \mathbf{u}_{FV}\frac{d_i}{d_e + d_i} + \mathbf{u}_{SPH}\frac{d_e}{d_e + d_i}. \quad (17)$$

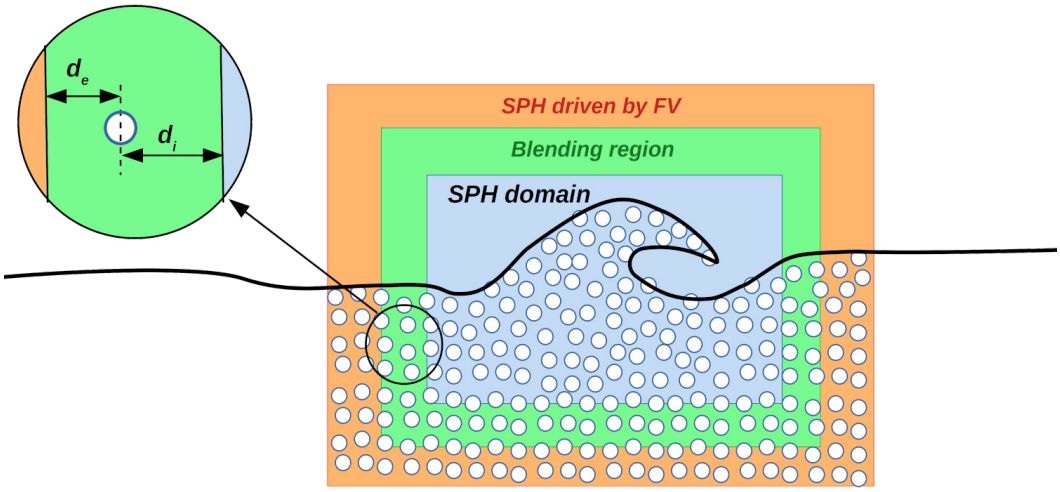

Fig. 2. SPH solution: blending region and region driven by FV

(3) In the outer region (orange in figure 2) the particle motion is driven by the velocity field computed in the underlying FV solution and interpolated on the instantaneous particle positions. This operation is made by tri–linear interpolation from the eight points of the Eulerian mesh that surround the particle; the donor points are found by the search algorithm described in [42].

Particle generation and removal

The outer boundary of the external region of the SPH domain lies in the FV domain: across this surface, particles are injected and removed on the basis of the flow direction and of the mass flow by means of an algorithm which is the natural extension to three dimensions of the one presented in [5] for two dimensional problems, as explained in the following. Each face of the outermost SPH domain boundary is split in sub–faces like in figure 3; from the FV solution, we compute the mass that flowed across each face element S_i from a reference instant of time t_0:

$$m_i(t) = \rho_0 \int_{t_0}^{t} \int_{S_i} \mathbf{u}(\hat{t}, \mathbf{x}) \cdot \mathbf{n} \, dS \, d\hat{t} \tag{18}$$

where $\mathbf{n}$ is the normal to the face element pointing inward the SPH domain and $\mathbf{u}(\hat{t}, \mathbf{x})$ is the value interpolated at the face center from the FV solution. The above integral is computed with second order accuracy in space by the mid-point rule and with first order accuracy in time. When this mass exceeds the reference particle mass $m_0 = \rho_0 V_0$, a new particle is injected and the value of the generated mass is subtracted from the instantaneous face mass, i.e. $m_i(t) \rightarrow m_i(t) - m_0$. Conversely, when this mass falls below $-m_0$, the closest particle to the face element is removed and its mass is summed to the instantaneous face mass.

The above procedure is applied for the face elements that are completely

submerged. When a face element is cut by the free surface, the mass flow is computed as

$$m_i(t) = \rho_0 \int_{t_0}^{t} \int_{S_i} \theta\left[-\phi(\mathbf{x}, \hat{t})\right] \mathbf{u}(\hat{t}, \mathbf{x}) \cdot \mathbf{n} dS \, d\hat{t} \tag{19}$$

θ being the Heaviside function and ϕ the signed distance (level set) function computed by the FV solver on the face element.

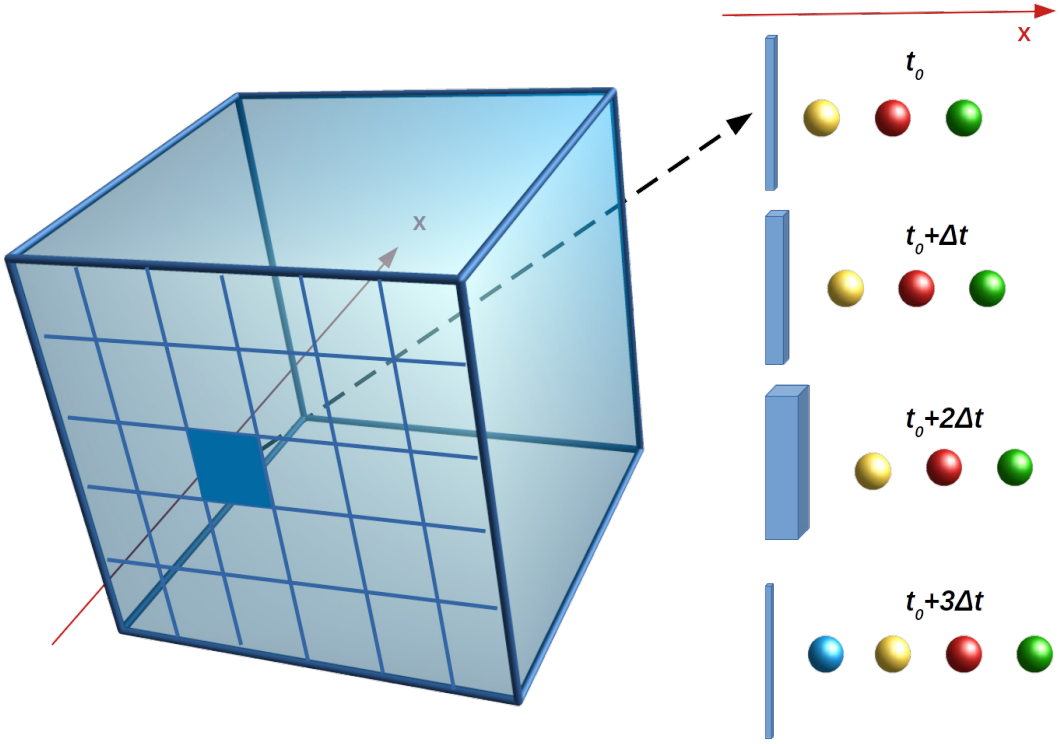

Fig. 3. Sketch of the particle injection algorithm.

The particles generated at the open boundary can suffer from spatial inhomogeneity when strong vortical structures move close to the boundaries; moreover, in the outermost region, where the particles are convected by the velocity field computed from the FV solver, spatial non uniformities can be caused by the exact Lagrangian transport law. This irregular particle distribution is controlled as done in [5] by means of the particle shifting technique as defined in equation (14).

Level set function computation

When coupling the SPH and FV solution, we need to transfer to the FV solver also the information regarding the distance from the free surface. This quantity is computed as in [25]: the particles on the free surface are detected by a purely geometrical criterion at first, and local unit normal vector to the free boundary $\mathbf{n}_{fs}$ is computed; then, the value of the signed distance function at a grid point $\mathbf{x}_{FV}$ of

the FV domain is computed from the closest free-surface particle at $\mathbf{x}_{fs}$ from

$$\phi(\mathbf{x}_{FV}, t) = (\mathbf{x}_{fs} - \mathbf{x}_{FV}) \cdot \mathbf{n}_{fs} - \frac{\Delta x}{2}. \tag{20}$$

Note that $\phi = -\Delta x/2$ at the particle center, the free surface being ideally located at a distance $\Delta x/2$ from the free-surface particle (see [25] for more details). In order to save CPU time, the level set function is computed only in the grid points of the FV domain adjacent to the free surface; in the other points, the level set function is computed by reinitialization at the beginning of each time step.

4.1.2 FV domain

As said before, two coupling approaches were tested in the present paper. The first one (*Coupling I* in figure 1) is the 3D extension of the approach in [26], i.e. the solution is transferred to the FV solver by interpolating the current SPH solution on two ghost cell layers adjacent to the inner boundary of the domain. The solution is interpolated on these cells by means of Shepard interpolation as explained for 2D problems in the cited papers.

In the second coupling approach (i.e. *Coupling II*), instead, the region occupied by the SPH particles is no longer removed from the FV domain; the two domains therefore overlap, as in figure 1. This second approach can be convenient because it produces a simpler algorithm at the price of a small overhead; moreover, the algorithm in this form can be extended with ease to the case of moving grid, as it will be done in the following of the research activity.

The solution is transferred from the SPH domain to the underlying FV domain by the same numerical technique adopted for solution interchange in the overlapping grid discretization as in [29] and [22]: in the cells overlapped by a SPH particles, the discrete equation are modified as

$$\begin{aligned} [LHS\ of\ eq.\ 4] + V_{i,j,k} \frac{K_\chi}{\delta_\chi} \left(\mathbf{u}_{i,j,k} - \mathbf{u}_{SPH} \right) = 0 \\ [LHS\ of\ eq.\ 5] + V_{i,j,k} \frac{K_\chi}{\delta_\chi} \left(\rho_{i,j,k} - \rho_{SPH} \right) = 0 \end{aligned} \tag{21}$$

where $K_\chi = O(10)$ is a non–dimensional constant and

$$\delta_\chi = min(\Delta t, \Delta x/U_{ref}, \Delta y/U_{ref}, \Delta z/U_{ref}) \tag{22}$$

U_{ref} being the reference velocity and $\mathbf{u}_{SPH}$ and ρ_{SPH} are the values of velocity and density from SPH at the point $\mathbf{x}_{i,j,k}$ obtained by interpolation from the SPH solver; these values are computed at grid points by means of the same interpolation technique (Shepard interpolation) adopted in the SPH solver. The same procedure

is applied for the computation of the level set function, i.e. a forcing term is added to equation (7)

$$\frac{\partial \phi}{\partial t} + \mathbf{u} \cdot \nabla \phi + \frac{K_\chi}{\delta_\chi} (\phi - \phi_{SPH}) = 0, \tag{23}$$

where ϕ_{SPH} is the value of the distance function computed from the SPH solver on each particle and transferred by a Shepard interpolation on each grid point.

4.2 Inhomogeneous time coupling

When coupling the two different solvers, we tried to exploit all the pre-existing coding of the algorithms, in order to use well consolidated software. The time integration of SPH being explicit and that of FV being implicit in the original implementation of the two algorithms, we adopted the inhomogeneous coupling procedure described in the following which is both consistent and stable (see [26] and [5]).

Suppose first that we chose the same time step Δt for SPH and FV; this is of course possible when Δt is equal to the limit time step for SPH, the FV algorithm being unconditionally stable. The time integration is performed first in the SPH region: to do this, we need the values from the FV in the overlapping region at the proper time instants, required for the Runge–Kutta multi-step integration. From the FV region we know the solution at the current time and, from the field equations, all the time derivatives for all the points in the overlapping region. Therefore, we can compute with second order accuracy all the values we need from a Taylor series expansion in the time interval $t^n < t < t^{n+1}$, t^n being the current time step and $t^{n+1} = t^n + \Delta t$:

$$\begin{aligned} \mathbf{u}_i(t) &= \mathbf{u}_i^n + \left.\frac{\partial \mathbf{u}}{\partial t}\right|_i^n (t - t^n) + O\left(\Delta t^2\right) \\ p_i(t) &= p_i^n + \left.\frac{\partial p}{\partial t}\right|_i^n (t - t^n) + O\left(\Delta t^2\right) \end{aligned} \tag{24}$$

On the other side, we need the solution at t^{n+1} in the overlapping region to perform the implicit integration of the FV domain. The required values are available once the Runge-Kutta integration on the SPH side is completed; therefore, no formal changes are required for the time integration in the FV domain.

If the time step Δt_{FV} for the implicit integration in the FV domain is chosen to be larger than the limit time step $\overline{\Delta t}_{SPH}$ for the SPH integration, the time marching procedure remains the same, but for each FV time step we make M steps with the SPH solver, M being the smallest integer for which the time step for the SPH solver Δt_{SPH} is such that

$$\Delta t_{SPH} = \frac{\Delta t_{FV}}{M} \leq \overline{\Delta t}_{SPH} \tag{25}$$

5 Numerical results

In this section, the three dimensional SPH-FV coupling is applied to some test problems with both the coupling procedures described above. Specifically, the proposed coupling strategy is applied and validated on complex 3D free-surface flows such as: i) the high-speed ditching of a flat plate; ii) the overturning wave generated by an advancing surface piercing plate; iii) the flow past a cylinder below the free surface. These problems are all chacterised by a large range of relevant spatial scales for which the present coupled approach can be effectively applied. In the following several numerical aspects are investigated such as the accuracy of the prediction of pressure fields, global forces, free-surface elevation and vorticity production.

Regarding convergence assessment of the present approach, in previous works by [26, 5] this aspect was extensively addressed. In particular, the convergence aspects regarding both space and time discretization were studied by using geometrically similar grids and particle distributions; the time discretization was such that the Courant number was kept constant on the different discretization levels. Furthermore, the sensitiveness of the solution on the ratio between typical particle and grid sizes was carefully analysed. Finally, the effect of the ratio between the time discretization of the two solvers was also addressed. Therefore, in the present work, we tried to focus more on the applicability of the coupling algorithm and due to the large computational costs required by the considered problems we could only perform uncertainty analysis on two different discretization levels for the test case of the flow past the cylinder underneath the free surface.

5.1 High speed water impact

In this section the ditching of a flat plate with large horizontal velocity component is studied; the SPH-FV coupled solutions are compared to fully-SPH solutions and to experimental data. Guided ditching impact experiments [14] were performed in the CNR-INM towing tank, which is 470 m long, 13.5 m wide and 6.5 m deep. The dimension of the flat plate were: width $W = 500\,mm$ and length $L = 1000\,mm$. L is taken as characteristic length for the problem. The horizontal and vertical velocities at the impact are respectively $U = 40\ m.s^{-1}$ and $V = -1.4\ m.s^{-1}$. Furthermore, the panel moves toward the free surface with a pitch angle of 10°. To mirror the experimental conditions, the ditching velocity is constant during the whole impact process.

SPH simulations of this problem have been previously performed in [24] using an Adaptive Particle Refinement (APR) technique as described in [6]. This advanced multi-resolution technique allows keeping fine spatial resolution around the flat

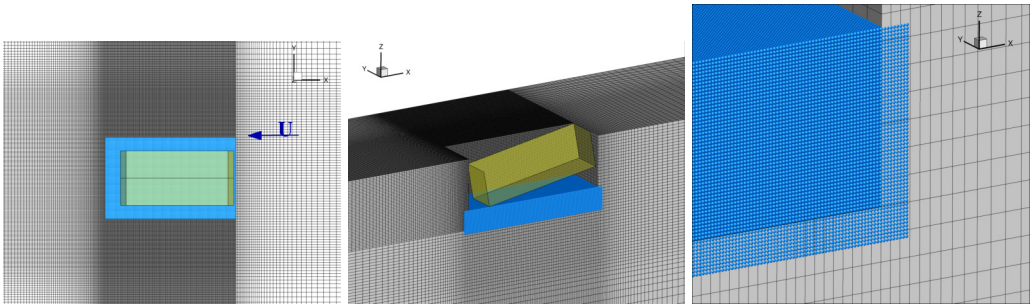

Fig. 4. High speed water impact: domain decomposition and adopted grids (SPH region is in blue). Left: top view. Middle: side view. Right: detail of the corner of the overlapping region between SPH and FV.

plate during the simulation by moving the refinement areas at the same speed of the plate. In the present study, the coupled SPH-FV solver has been tested on the same problem in order to assess pros and cons of the proposed technique for water impact problems.

Simulations have been performed with a nominal sound speed $c^{water} = 1480\,m/s$ and a nominal density $\rho_0^{water} = 1000\,kg/m^3$ for water. Viscous effects have been neglected due to the high Reynolds number of the flow in this impact situation. The problem is solved in a frame of reference which is moving with the same horizontal velocity as of the plate. In this system, the plate moves purely downward with velocity V, whereas the flow velocity in the far field is $\mathbf{u}_{inflow} = (U, 0)$. The numerical tank is $10\,m$ long, $3\,m$ wide and $6\,m$ deep.

The SPH domain is around the plate and is $1.25\,m$ long, $0.8\,m$ wide and $0.2\,m$ deep. The depth of the SPH domain was set large enough to include the region around the moving plate during the whole simulation in the time interval $[0, tU/L = 3.5]$. For this problem, the first coupling technique (*Coupling I*) was adopted; the complement to the SPH domain is covered by the FV mesh, with grid stretching in the far field.

The adopted SPH and FV domains are depicted in left and middle plots of figure 4. In the right plot of figure 4 a detail of domain overlapping is shown, with at least two FV cells falling in the SPH region and a layer of SPH particles corresponding to at least one kernel radius lying in the FV domain.

Flat panel impact: comparison between coupled SPH-FV and SPH alone

SPH-FV simulations were performed using a particle resolution $\Delta x = 3.2\,mm$ which is very close to minimum particle size that was adopted in [6] corresponding to $\Delta x = 3.125\,mm$. The total amount of particles at the beginning of the simulation is 6 millions, whereas the total number of FV cells is about 4 millions. It has to be noted that the number of SPH particles could be drastically reduced if the SPH box was able to move with the plate (this will be done in the continuation of this

research activity).

As regards the time integration, the SPH time step is defined by the acoustic CFL condition and is equal to $\Delta t_{\mathrm{SPH}} = 2.5 \times 10^{-6} s$ whereas there is no restriction on the FV time step for stability, the FV being fully implicit in time. Nevertheless, the accuracy analysis performed in [26] suggests to limit its value to $10 \times \Delta t_{\mathrm{SPH}}$.

The top plot of figure 5 shows the field of the pressure coefficient $C_p = P/[1/2\,\rho_0\,(U^2 + V^2)]$, where U and V are the reference velocity components of the flat plate. The figure reports C_p on a particle slice at the plate midline as predicted by the SPH-FV solver and by the SPH alone in [24] at $t = 1.6\,tU/L$. It can be observed that the pressure levels are very similar; nevertheless, the SPH-FV solution is much smoother and free from oscillations with respect to the simulation using SPH alone. This can be attributed to the fact that a perturbation produced in the SPH region is efficiently damped in the far field by the FV solver, without bouncing back in the near field. In the middle row of figure 5 the top view of the pressure field at the solid boundary is shown. From this plot the similarity between the two pressure fields can be further appreciated, together with the smoothness of the SPH-FV solution. In particular, the parabolic shape of the high-pressure region at the jet root, which is due to the jet escaping from the lateral sides, is well represented in both solutions.

At bottom plots of figure 5, the contours of the free-surface elevation are reported. In this picture, an abrupt discontinuity in the free surface elevation clearly appears at the side boundaries of the outer SPH domain in the SPH-FV solution. This is to be ascribed to the fact that the SPH resolution is much higher than the FV one in the interface region, where the emerging liquid jet is very thin (about one particle thick in the SPH simulation). This tiny detail can not be captured by the FV grid and, as a consequence, the jet disappears when entering in the FV region. However, it is important to underline that this aspect has no consequences on the loads on the plate and on the overall impact process, nor on the stability of the algorithm.

Finally, in figure 6 the vertical force measured on the plate is compared between the two numerical solutions and with the experimental measurements. The numerical solutions are in good agreement and both slightly overestimate the experimental data. When inspecting more in the detail the numerical signals, it can be observed that the SPH-APR solution (in blue) is affected by a small high-frequency noise, as expected from the reported pressure fields. Conversely, the SPH-FV solution is in general very smooth, apart from the initial stage of the impact and some bumps towards the end of the simulation. The first oscillations are due to the initial deformation of the particle lattice which induces some noise due to the limited resolution at the initial jet root, present in both numerical solutions.

The second effect is more tricky: as the wedge penetrates the liquid, the mean water level rises and a new layer of particles is generated from the inflow. Due to the rapid

flow, this new particle line remains in the shape of a small step on the free surface until it encounters the plate. This induces a local small pressure bump at the jet-root. However, this spurious effect could be quickly alleviated by introducing a particle shifting tangential to the free surface, as in [38].

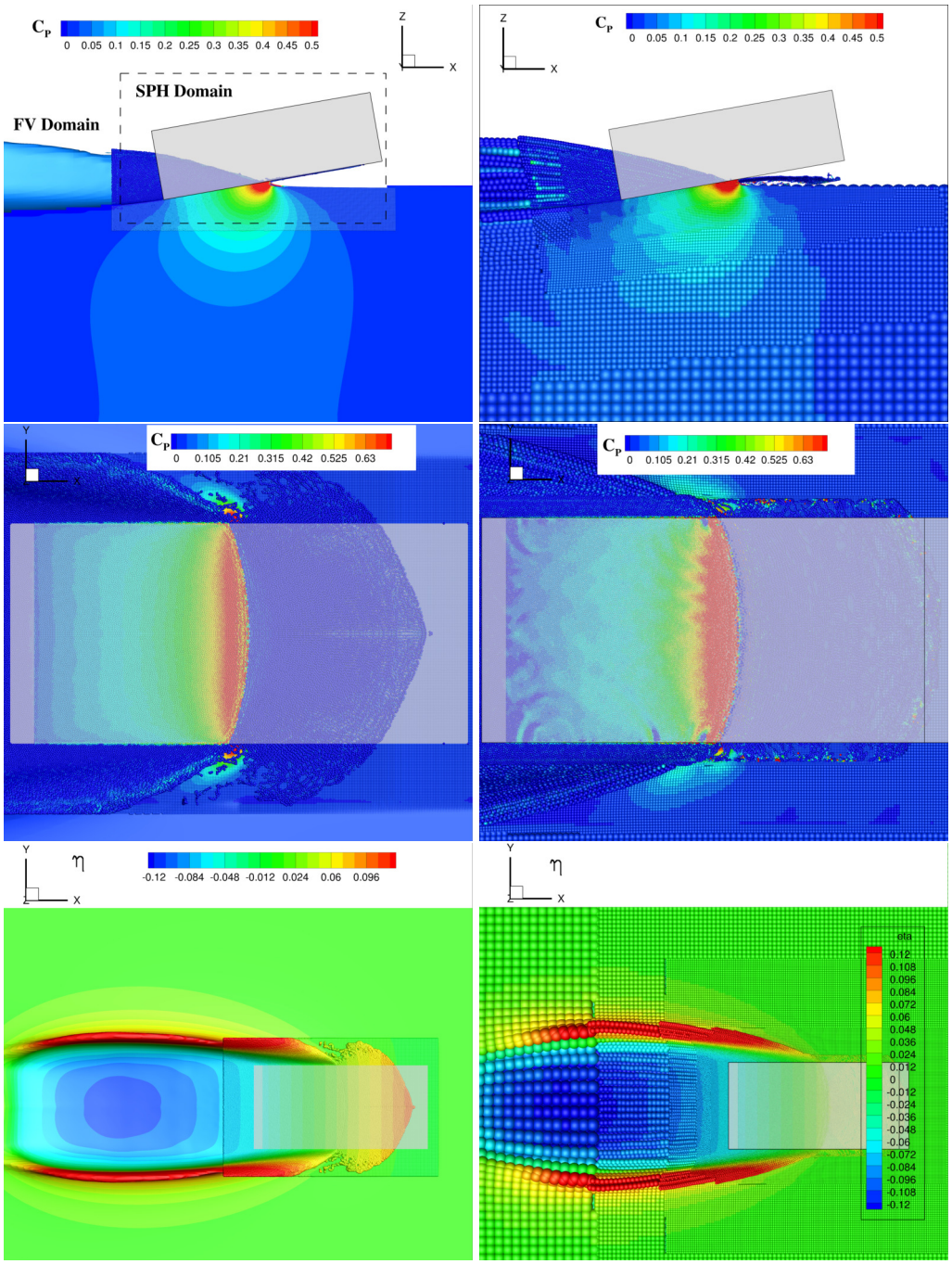

Fig. 5. High speed water impact: solution at $t = 1.2\,tU/L$. Top: side view of the pressure coefficient C_P; middle: top view of the pressure coefficient C_P; bottom: free surface elevation. Left: SPH-FV coupled solution. Right: solution by SPH with APR from [24].

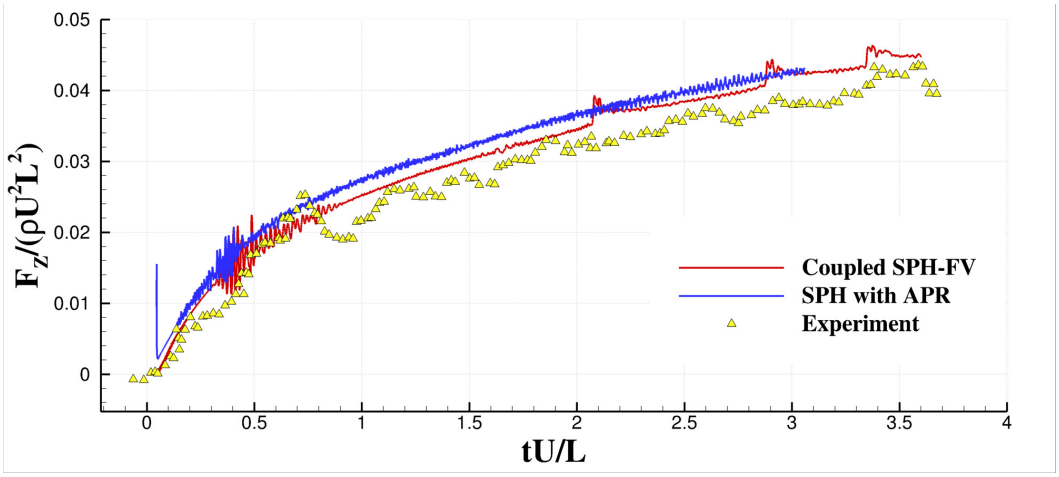

Fig. 6. High speed water impact: vertical forces acting on the plate during the impact. Triangles represent the force recorded in the experiment by [14]; the red and blue lines represent the force measured, respectively, in the SPH-FV and in the SPH with APR simulations.

5.2 *Overturning ship-like bow wave*

The coupled solver is here validated on the problem of a ship-like breaking bow wave generated by an advancing free-surface piercing plate. The experimental campaign carried out in the Ecole Centrale de Nantes towing tank reported in [33] and [8] is here taken as reference. The considered problem is quite challenging when tackled by either SPH or FV alone. Indeed, from the point of view of the SPH solver, the fluid domain to be simulated is too large; from a FV perspective, too high resolution would be needed to solve the details of the overturning breaking wave.

The problem is defined as follows: a rectangular plate of length $L = 0.782$ m is immersed with a draught equal to $D = 0.2$ m and towed with different velocity U and incidence (yaw) angle α. The yawed plate generates an overturning wave which resembles the one produced by a ship bow in forward motion.

In this section, the solutions obtained through the coupled solvers are compared with the experimental data in terms of wave shape and maximum wave height on the plate. A sketch of the problem and of the discretization is reported in the left plot of figure 7: the SPH region, indicated by the red parallelepiped, is attached to the upper part of the plate to catch the breaking wave, while the FV region occupies the remaining part of the domain, in order to resolve the far field, the recirculating flow behind the plate and the vorticity generation at the immersed edge of the plate.

For the solution of this problem we adopted *Coupling II*, as explained in section 3. Specifically, the FV overlapping grid is shown in figure 7, where a top view of the numerical domain is provided; for the sake of clarity only every second point of the grid is plotted. Very coarse grids are used in the far field in order to rapidly damp the outgoing perturbations and avoid spurious reflections. A finer grid is used on the plate with clustering at the wall, in order to resolve the boundary layer. Indeed, for the flow velocity considered here, the first point is set at a distance $O(10^{-5})$ m from the wall, so that the distance of the closest point from the wall is always below 1 in terms of wall units; note that this spatial resolution is not reachable by any SPH scheme with common computers.

The boundary layer is solved by FV, the FV grid resolution being at least two orders of magnitude finer than the SPH one; conversely, outside the boundary layer the solution is driven by SPH which is far more convenient in order to catch the free surface evolution. The SPH domain covers the whole plate length and spans up to $y = 0.5L$ in the direction perpendicular to the plate; on the contrary, the depth is only $0.06L$ below the undisturbed free surface, since the free surface mainly evolves above it. The adopted particle size is $\Delta x = 0.003L$, resulting in about 1 million particles at the beginning of the simulation. Note that, during the evolution, the water rise in front of the plate causes a large increase of this number, leading

to an average particle number even 4 times larger than the initial one. For all the simulations of this section the thickness of the blending region is about $3\Delta x$ as well as the region of pure FV forcing (see figure 1 for definitions).

Since in this problem the acoustic waves are not of interest, the chosen time step for the FV solver is $\Delta t_{FV} \simeq 10\Delta t_{SPH}$. From the point of view of the computational cost, for this test case one time step of the FV solver is about 20 times more expensive than one SPH step, the FV grid being also larger than the SPH one. Therefore, taking into account the time step ratio, the FV burden on the total CPU cost is about twice the SPH one. Each simulation ran on a 48-cores Intel Xeon CPU E5-2698 2.30GHz machine for about 96 hours in order to simulate 8 seconds of physical time.

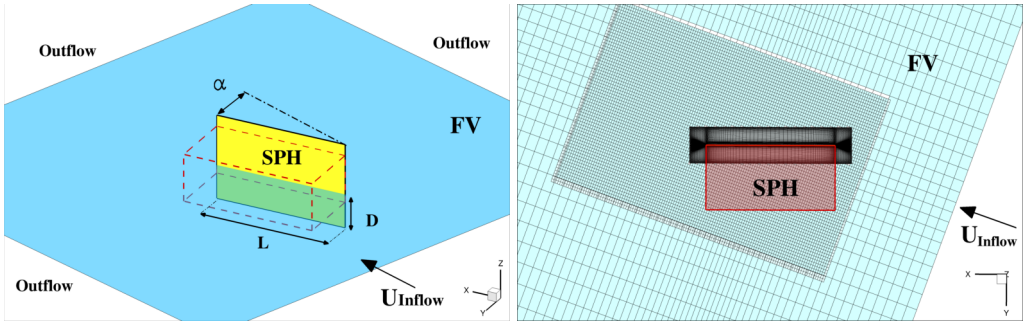

Fig. 7. Overturning bow wave. Left: sketch of the problem. Right: computational domain, subdomains and boundary conditions. Every second point is represented in the FV grid.

In figure 8 two different views of the solution at $tU/L = 7$ obtained for Froude number $\mathrm{Fr}_D = U/\sqrt{gD} = 1.07$ are reported in terms of free-surface elevation contours, in both SPH and FV domains. It can be seen that, when the flow encounters the plate, the stream forks between the high-pressure region (solved by SPH) and the low-pressure one; on the high-pressure side, the flow climbs the plate, and falls back in the form of a plunging breaking wave, whose shape depends on the flow velocity. The overturning wave attains a quasi-steady regime after a short transitory stage which ends at about $tU/L = 3$. In the case shown in figure 8, a small plunging wave is formed which evolves in a series of splash-ups, thus dissipating its initial energy content.

The plunging jet impinging the free-surface divides in two parts: a portion of it penetrates the surface and another one bounces in the form of a new jet (for more details see e.g. [21]). As a result a vortical structure is generated beneath the water which runs parallel to the plate, in a way that resembles the “scars” observed in the wake of ship bow waves (see [17]). These scars are clearly visible in the SPH region in the top view of figure 8; these small scale structures are blurred when they reach the FV domain, the grid size being insufficient to describe their details. When the splashing wave reaches the lateral limit of the SPH region most of the energy has been damped through vorticity and water impacts (see e.g. [23] and passes in the FV domain. As for the “scars”, FV grid resolution is not enough

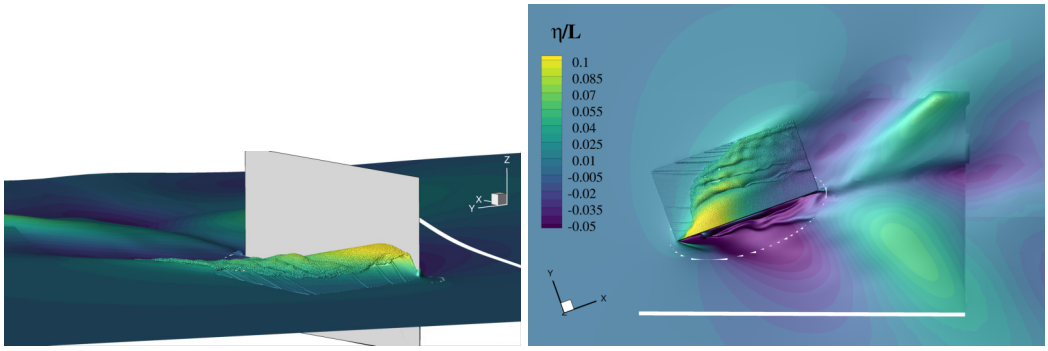

Fig. 8. Overturning bow wave: numerical solution obtained by the coupled SPH-FV solver for $\mathrm{Fr}_D = 1.07$. Free-surface elevation viewed from the front plane (left plot) and from the top (right plot). Colors refer to the free-surface perturbation with respect to its undisturbed configuration.

to capture small breaking events, and therefore are damped. Consequently, only a smooth free-surface deformation is captured by the coarse FV grid.

The results from the simulation are compared with experimental data for validation for several values of the Froude number and incidence angle α. The validation is carried out by comparing the free surface elevation along the plate and the features of the breaking wave. In figure 10 the computed waves (on the left) for $\mathrm{Fr}_D = 1.07$ and $\alpha = 10°, 15°, 20°, 25°, 30°$ are compared with the photos taken from experiments in the towing tank (on the right). For visualization purposes, the SPH solution is shown in terms of triangulated surface, extracted through a marching cube algorithm, and the experimental free-surface elevation has been reported on the numerical solution using red points.

The observation of figure 10 clearly reveals the influence of the incidence angle α on the wave shape. At $\alpha = 10°$ the wave is at its breaking limit and the comparison with experimental data proves that the computed wave profiles are in very good agreement with the experiment. At $\alpha = 15°$ the overturning wave is now well formed and the SPH accurately predicts the generation of the overturning wave. In this case both the computed wave profile and shape are in good agreement with towing tank observation; moreover, the numerical simulation well captures the closure point of the overturning wave. A similar behaviour is observed also for $\alpha = 20°$ for which the breaking wave is more curved and the jet impingement occurs closer to the plate. In this case the splash-up is also well visible.

At $\alpha = 25°$ and $\alpha = 30°$ the overturning wave is not clearly visible any more as it closes just aside the plate. However, it can be noticed that for $\alpha = 30°$ in the numerical solution the first scar line induced by the splash-up is visible, running almost parallel to the plate. Remarkably, a similar behaviour can be spotted also in the experimental picture. As far as the free-surface profile is concerned, for these cases the water elevation is rather unsteady and, thus, the comparison is less precise. In general, the numerical solution is close to the experimental data in the front part

while it slightly overestimates the water elevation downstream.

In order to validate the numerical solution when varying the Froude number, in figure 9 the computed maximum wave height is compared with the experimental data and with the theoretical estimation in [32]

$$Z_b \frac{g}{U^2} = \frac{2.2}{1 + Fr_D} \frac{\tan \alpha}{\cos \alpha} \tag{26}$$

where Z_b is the maximum wave height. From the picture in figure 9 it can be seen that the numerical simulation lays within the experimental scattering; both experiments and simulations are slightly below the theoretical maximum wave height.

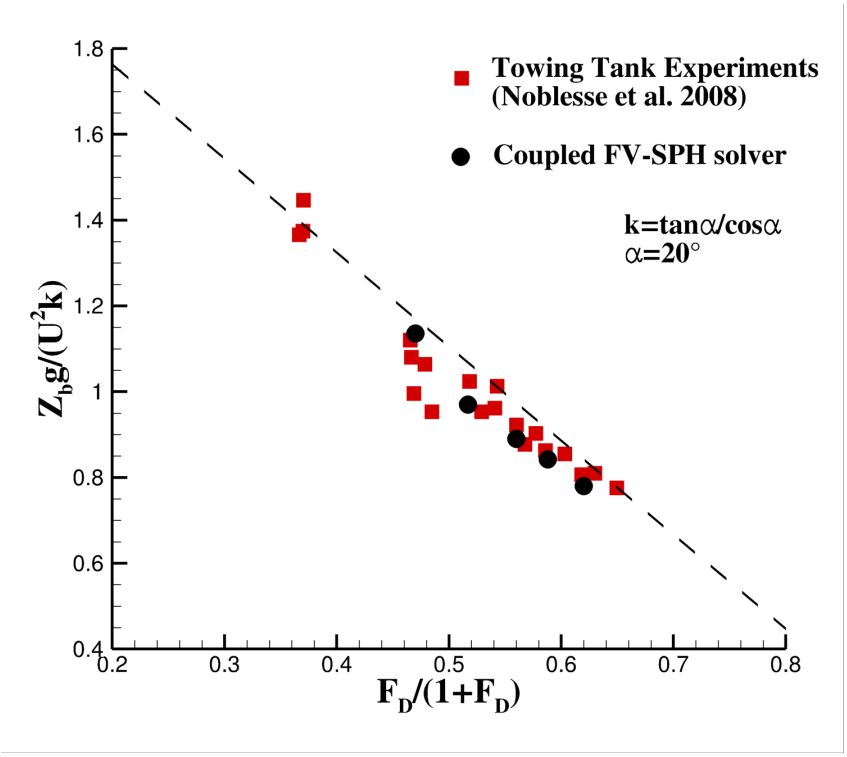

Fig. 9. Overturning bow wave: comparison of the computed maximum wave height for varying Froude number with experimental data and with analytical law in [32]

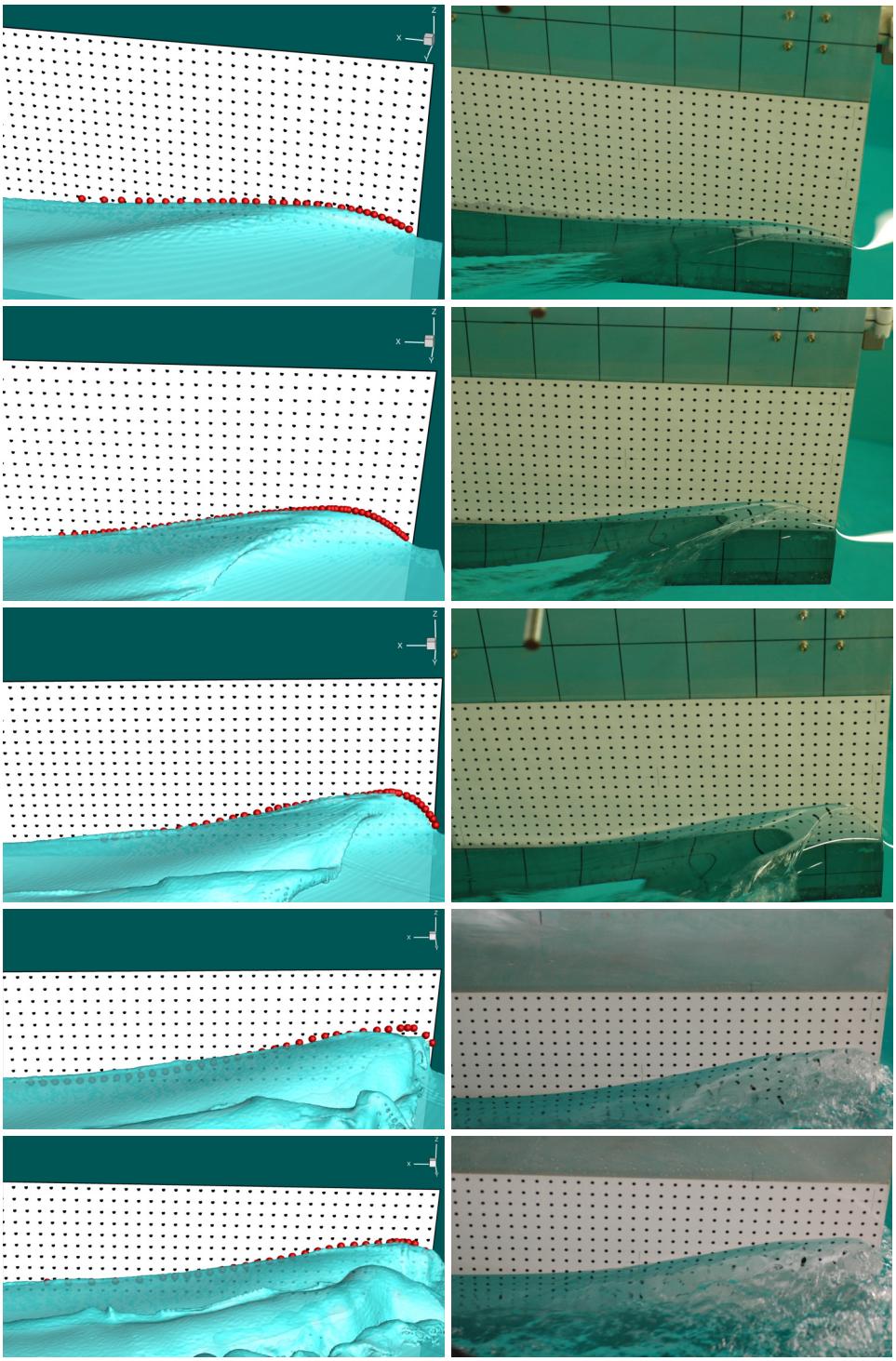

Fig. 10. Overturning bow wave: detail of the bow wave varying the incidence angle α at $\mathrm{Fr}_D = 1.07$. From top to bottom: $\alpha = 10°, 15°, 20°, 25°, 30°$. Left: numerical solution by SPH-FV solver; the red spheres represent the wave profile measured in the experiment. Right: pictures taken from the experiments.

5.3 Flow past a circular cylinder below a free surface

In the present section the viscous flow around a cylinder below a free surface is computed. The problem is the 3D extension of the 2D problem solved in [5] and consists of an open channel with a fixed cylinder beneath the free surface. The same test case was studied in [3] and, more recently, in [7]. A section of the adopted domain is shown in Figs. 11 and 12; note that in the global view of the domain only every fourth FV grid point is shown for the sake of clarity.

The problem is characterized by:

- distance between free surface and cylinder (h) / cylinder diameter (d): $h/d = 1.5$;
- water depth ($\hat{H}$) / cylinder diameter: $\hat{H}/d = 6$;
- Froude number $\mathrm{Fr} = U/\sqrt{gd} = 1$, g being the gravity acceleration and U being the inflow velocity;
- Reynolds number $\mathrm{Re} = Ud/\nu = 180$ and 1800, ν being the kinematic viscosity;
- free-slip condition at the bottom and no-slip condition on the cylinder wall;
- distance of inflow boundary from the cylinder (x_1) / cylinder diameter: $x_1/d = 21$;
- distance of outflow boundary from the cylinder (x_2) / cylinder diameter: $x_2/d = 59$.

The 3D extension considered here is obtained by extruding the domain of figure 11 for a length equal to $3d$ and enforcing periodic boundary conditions at the planes $y = -1.5d$ and $y = 1.5d$. The flow evolves producing a spilling breaking wave above the cylinder as a result of the accelerating current close to the free surface. The domain decomposition is such that only the portion of the region around the breaking wave is discretized by SPH (see Fig. 12). For the remaining part of the domain a Chimera-type grid was adopted which is composed by orthogonal sub-grids, properly clustered around the cylinder and stretched far away from it The total number of cells is about 3 millions. The particle resolution for this case is $d/\Delta x = 33$, amounting to an average total particle number of about 1.3 millions (the number of particles inside the domain slightly changes in time due to the flow unsteadiness). The adopted FV time step is $\Delta t U/d = 0.0125$ which is approximately 5 times the SPH time step. For this simulation, *Coupling II* was adopted, i.e. the complete FV grid is overlapped by the SPH domain.

5.3.1 Flow at Re=180

After an initial transient stage, the flow reaches a quasi-periodic regime with period $tU/d \sim 5$. A peculiar element of this flow is the mutual interaction between vortex shedding in cylinder wake and the breaking waves. This aspect was deeply investigated in [3, 7]. In figure 13 the x-component of the velocity field is reported. At this Reynolds number (Re=180) the flow remains nearly two-dimensional. It

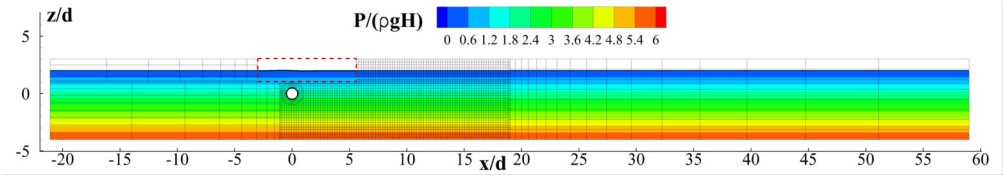

Fig. 11. Flow past a circular cylinder below a free surface - Section of the 3D computational domain, subdomains and initial configuration. Every fourth point is represented in the FV grid.

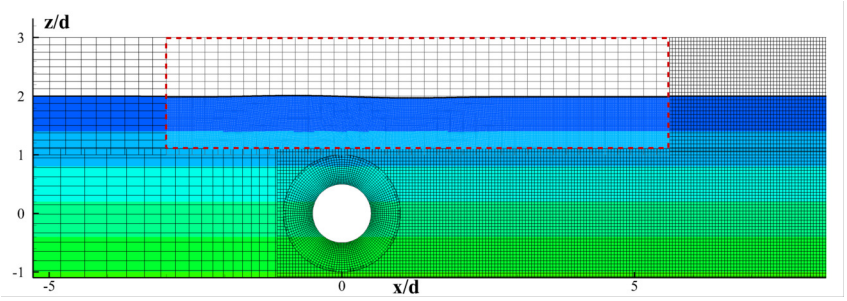

Fig. 12. Flow past a circular cylinder below a free surface - Zoom of the SPH sub-domain delimited by the red-dashed box.

is worth noting the field continuity and smoothness across the interface between SPH and FV, which can be better appreciated in the zoomed view in bottom plot of figure 13. Also the free surface is quite accurately transferred from one domain to the other, even in the region downstream the breaking wave, where small 3D effects can be spotted.

In figure 14 the y-component of the vorticity field is reported. In the bottom plot the same field obtained from a 2D simulation in [5] is reported. Since the flow is practically 2D, the two solutions are in very good agreement both in terms of vorticity distribution and free-surface deformation, in spite of the different type of coupling algorithm adopted for the two simulations.

In order to assess the uncertainty a two-grid approach was adopted [37]. A coarser grid for the FV solver was obtained by removing every other grid point from the original grid. As for the SPH resolution, the particle size was doubled, i.e. $d/\Delta x = 16.5$. The obtained grids are, respectively, of about 440,000 FV points and 160,000 SPH particles. Moreover, the Courant number was kept constant. A further coarsening of the grid would have resulted into a too rough description and was not used. The results are reported in table 1 in terms of average lift and drag coefficients, namely C_L and C_D. As it can be seen the observed uncertainty for both quantities is below 5%.

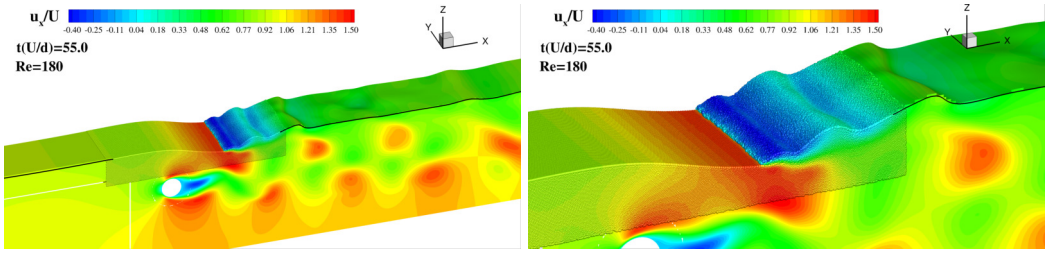

Fig. 13. Flow past a circular cylinder below a free surface at Re=180. Left plot: side view of the x-component of the velocity field; right plot: zoomed view close to the SPH region.

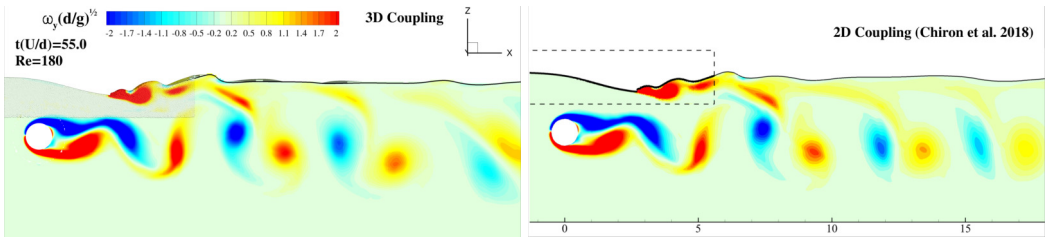

Fig. 14. Flow past a circular cylinder below a free surface at Re=180. Left plot: side view of the y-component of the vorticity field; right plot: vorticity field in the 2D solution provided in [5].

	C_D	C_L
Grid 1	1.54	−0.081
Grid 2	1.49	−0.078
Unc. %	3.2	3.7

Table 1
Flow past a circular cylinder below a free surface at Re=180 - Uncertainty assessment.

5.3.2 Flow at Re=1800

As a second test case the same simulation is performed at a viscosity level 10 times lower, i.e. with Re=1800; the Froude number is the same as before Fr $= U/\sqrt{gd} = 1$. In order to correctly model the boundary layer, the grid close to the cylinder wall is further refined so that the first computation point is at $y^+ \simeq 1$. For this second test case the total number of cells is about 3.5 millions. Note that such a resolution would be practically unfeasible using only SPH, even with advanced particle splitting techniques such as, e.g., the Adaptive Particle Refinement [6]. The particle resolution in the SPH region is also increased to $d/\Delta x = 50$ in order to better describe the complex free surface evolution. The total particle number is about 4.5 millions. Again, in case only FV was used a very large number of points would have been needed, since all the volume which can be potentially occupied by the free surface must be resolved with a very fine discretization.

In figure 15 the contour plot of the x-component of the velocity field of the obtained flow is shown for $tU/d = 90$. At this time instant the initial transient has passed

and the flow exhibits an irregular wake. The free surface has remarkable 3D effects, with several breaking waves that are more violent than in the previous case with Re = 180. In top plot of figure 16 a zoom of the free surface across the interface is presented. The SPH particles and FV surface are colored according to the elevation of the surface. It is possible to observe that the surface elevation across the coupling interface is continuous, even if complex three-dimensional surface perturbations are present.

In middle and bottom plots of figure 16, two views of the vortex structures are provided. The vortex surfaces are defined through Q-criterion [15] and in particular are obtained as iso-surfaces at $Q(d/U)^2 = -1$, where Q is defined as:

$$Q = ||\mathbb{E}||^2 - ||\Omega||^2$$

$\mathbb{E}$ and Ω being, respectively, the symmetric and skew-symmetric parts of the velocity gradient tensor. Note that Q is computed also on particles and in figure 16 only particles characterized by $Q(d/U)^2 \leq -1$ are plotted in yellow. From the bottom view it can be seen that at this Reynolds number the flow develops strong 3D effects also close to the cylinder: the vortex structures of the von Karman street are connected through orthogonal filaments which interacts with the free surface. Indeed, particles detected by Q-criterion are visible in the shape of filaments just below the free surface. In the bottom plot of figure 16 vortex structures can be observed also across the interface. This represents a remarkable result of the proposed algorithm, as the computed fields remain continuous also in terms of derived quantities, such as the Q value. Furthermore, from this plot it is visible how the vorticity generated at the free surface interacts with the vortex structures produced on the cylinder wall: small vortices generated by the breaking wave merge with vorticity coming from the cylinder below and remain close to the free surface, causing also significant local deformation of the latter.

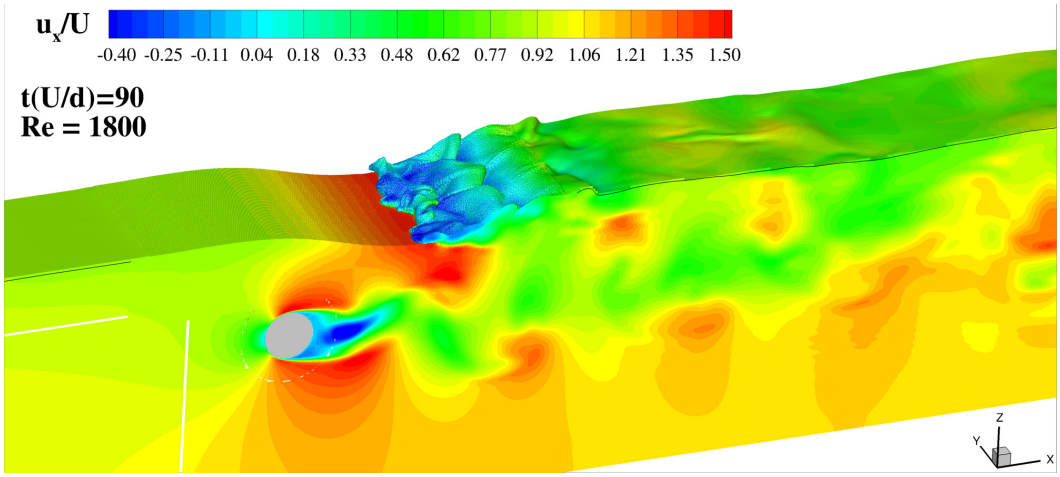

Fig. 15. Flow past a circular cylinder below a free surface at Re=1800: side view of the x-component of the velocity field.

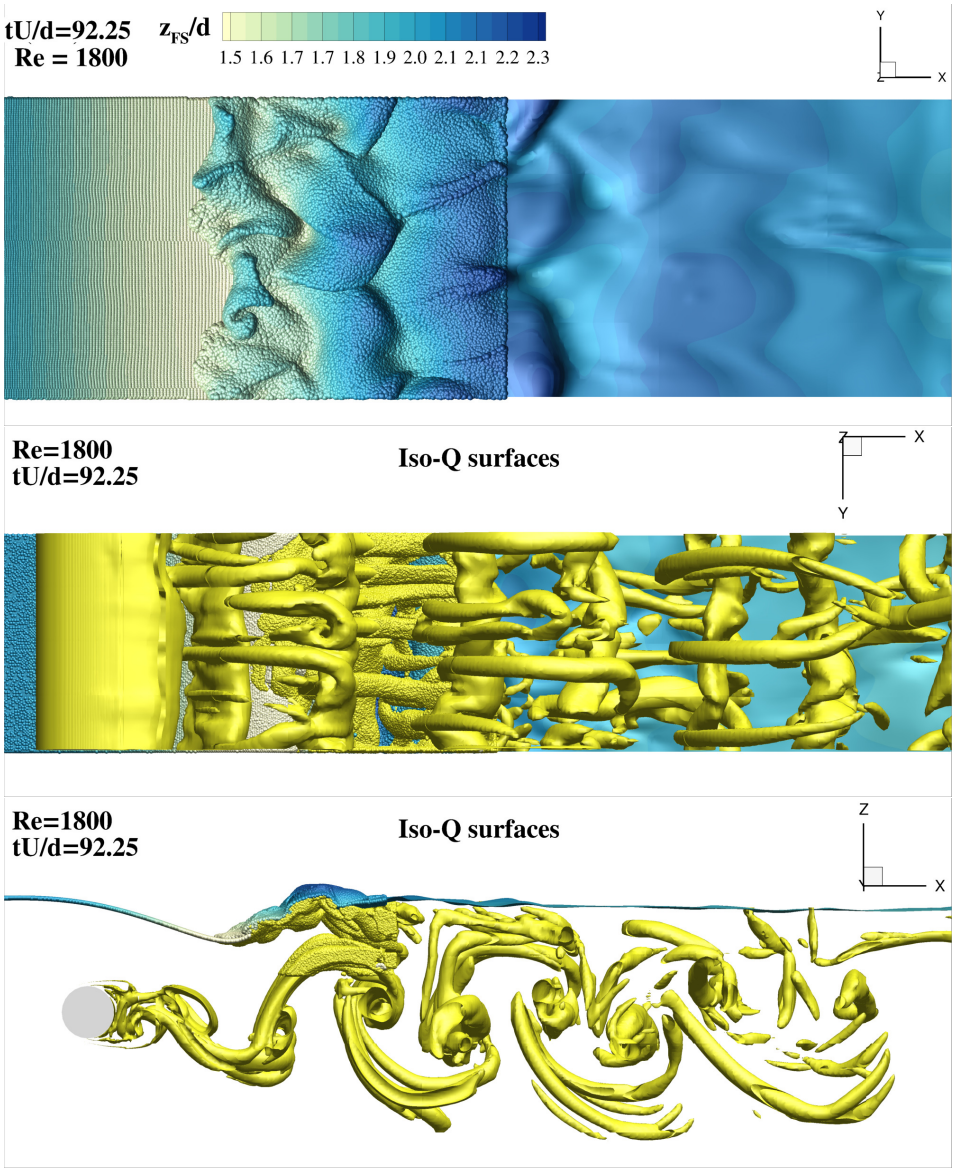

Fig. 16. Flow past a circular cylinder below a free surface at Re=1800. Top plot: top view of the free surface close to the interface between SPH and FV; colors refer to free-surface elevation. Middle plot and bottom plot: bottom and side views of the vortex structures represented as iso-surfaces at $Q(d/U)^2 = -1$ (SPH particles characterized by the same value of Q are also shown).

Conclusions

A 3D algorithm for the solution of free surface problems with both free-surface fragmentation and relevant viscous effects is proposed. The algorithm extends and improves the one developed for 2D flows in [26] and [5]; a new and simpler paradigm to couple a Smoothed Particle Hydrodynamics solver and a Finite Volume one with Level Set approach is also developed and implemented; with this new algorithm, grid generation follows the usual practice of Finite Volume approaches because there is no need to remove grid portions or to define additional internal boundaries.

Three test cases were considered to test both versatility and robustness of the algorithm. In the first, the impact of an inclined flat plate on the water surface is considered, to check acoustic wave propagation through the interface: the test revealed the smooth propagation of both acoustic waves and free surface front between the two domains; moreover, the computed pressure on the plate surface favourably compares with both experiments and with an analogous computation performed with a pure SPH solver.

In the second test case, the overturning wave induced by a yawed surface piercing flat plate is simulated. This test case is severe for both solvers when used alone: in fact, the SPH solver easily captures the plunging or spilling waves that characterize the problem, but misses the boundary layer and the vortices generated at the keel and on the trailing edge. Conversely, when using the FV solver, boundary layers and wakes can be easily captured by proper grid stretching and local refinements, while the proper description of the surface wave would require an excessively fine grid in the region around the front evolution. The numerical results obtained with the new coupling approach accurately mirror the data collected in a towing tank experiment.

The third test case reported offers the same difficulties as the second one. The 3D flows around a circular cylinder placed underneath the free surface is simulated for low and high Reynolds number with the new coupling procedure. For the low Reynolds number case, the solution remains almost 2D and perfectly mirrors the 2D results obtained before with the first coupling approach proposed. The flow obtained with the higher value of the Reynolds number is instead fully 3D and encompasses the typical vortex structures in the wake of the cylinder that interact with both the vorticity produced under the breaking wave and with the free surface.

The proposed algorithm, although very convenient in terms of accuracy and CPU reduction, of course add complexity to the setup of the numerical simulation and requires additional skill and experience by the user. A way to overcome this hindrance could be to inspect the level-set function in a preliminary coarse FV simulation and identify the regions where SPH would be more effectively used.

Then, the simulation setup could greatly simplified by the development of an efficient and automatic dynamic domain decomposition approach which would relieve the user from the need of a complex domain cutting. Such an algorithm would be useful also for the extension to moving body problems and multi-phase flows. Furthermore, we are going to implement the coupled approach for flows such that the LES modelling is feasible. For the FV several turbulence models are already available whereas for the SPH the δ-LES-SPH scheme recently proposed by [11, 1] may be used. In this last case an additional field has to be exchanged at the interfaces as, *e.g.*, the turbulent viscosity.

Acknowledgements

The research leading to these results has partially received funding from the European Union's Horizon 2020 research and innovation programme under grant agreement No 724139.

Authors are thankful to their former colleague from Ecole Centrale Nantes, Dr. Gérard Delhommeau, for his help regarding the towed plate experimental data.

The SPH simulations performed under the present research have been obtained using the SPH-Flow solver, software developed within a collaborative consortium composed of Ecole Centrale de Nantes, NEXTFLOW Software company and CNR-INM.

References

[1] M Antuono, S Marrone, A Di Mascio, and A Colagrossi. Smoothed particle hydrodynamics method from a large eddy simulation perspective. generalization to a quasi-lagrangian model. *Physics of Fluids*, 33(1):015102, 2021.

[2] B. Bouscasse, S. Marrone, A. Colagrossi, and A. Di Mascio. Multi-purpose interfaces for coupling SPH with other solvers. In *Proceedings of the 8th International SPHERIC Workshop*, 2013.

[3] Benjamin Bouscasse, Andrea Colagrossi, Salvatore Marrone, and Antonio Souto-Iglesias. SPH modelling of viscous flow past a circular cylinder interacting with a free surface. *Computers & Fluids*, 146:190–212, 2017. ISSN 0045-7930. doi: 10.1016/j.compfluid.2017.01.011. URL `//www.sciencedirect.com/science/article/pii/S0045793017300245`.

[4] Fuzhen Chen, Hongfu Qiang, and Weiran Gao. Coupling of smoothed particle hydrodynamics and finite volume method for two-dimensional spouted beds. *Computers & Chemical Engineering*, 77:135–146, 2015.

[5] L Chiron, Salvatore Marrone, Andrea Di Mascio, and David Le Touzé. Coupled SPH–FV method with net vorticity and mass transfer. *Journal of Computational Physics*, 364:111–136, 2018.

[6] Laurent Chiron, Guillaume Oger, Matthieu De Leffe, and David Le Touzé. Analysis and improvements of Adaptive Particle Refinement (APR) through CPU time, accuracy and robustness considerations. *Journal of Computational Physics*, 354:552–575, 2018.

[7] A Colagrossi, G Nikolov, D Durante, S Marrone, and A Souto-Iglesias. Viscous flow past a cylinder close to a free surface: Benchmarks with steady, periodic and metastable responses, solved by meshfree and mesh-based schemes. *Computers & Fluids*, 181:345–363, 2019.

[8] Gerard Delhommeau, Michel Guilbaud, Laurent David, Chi Yang, and Francis Noblesse. Boundary between unsteady and overturning ship bow wave regimes. *Journal of Fluid Mechanics*, 620:167–175, 2009.

[9] A Di Mascio, R Broglia, and R Muscari. On the application of the single-phase level set method to naval hydrodynamic flows. *Computers & fluids*, 36 (5):868–886, 2007.

[10] A. Di Mascio, R. Muscari, and G. Dubbioso. On the wake dynamics of a propeller operating in drift. *Journal of Fluid Mechanics*, 754:263–307, 2014.

[11] A Di Mascio, M Antuono, A Colagrossi, and S Marrone. Smoothed particle hydrodynamics method from a large eddy simulation perspective. *Physics of Fluids*, 29(3):035102, 2017.

[12] Andrea Di Mascio, Riccardo Broglia, and Roberto Muscari. Prediction of hydrodynamic coefficients of ship hulls by high-order Godunov-type methods. *Journal of Marine Science and Technology*, 14(1):19–29, 2009. ISSN 0948-4280. doi: 10.1007/s00773-008-0021-6.

[13] Douglas Enright, Ronald Fedkiw, Joel Ferziger, and Ian Mitchell. A hybrid particle level set method for improved interface capturing. *Journal of*

Computational Physics, 183(1):83–116, 2002.

[14] A Iafrati. Experimental investigation of the water entry of a rectangular plate at high horizontal velocity. *Journal of Fluid Mechanics*, 799:637–672, 2016.

[15] Hunt' JCR, A Wray, and P Moin. Eddies, stream, and convergence zones in turbulent flows. *Studying Turbulence Using Numerical Simulation Databases-I1*, 193, 1988.

[16] Petros Koumoutsakos. Multiscale flow simulations using particles. *Annu. Rev. Fluid Mech.*, 37:457–487, 2005.

[17] M. Landrini, A. Colagrossi, M. Greco, and M.P. Tulin. The fluid mechanics of splashing bow waves on ships: A hybrid BEM-SPH analysis. *Ocean Engineering*, 53(0):111–127, 2012. ISSN 0029-8018. doi: 10.1016/j.oceaneng.2012.06.027. URL http://www.sciencedirect.com/science/article/pii/S0029801812002314.

[18] S.J. Lind, R. Xu, P.K. Stansby, and B.D. Rogers. Incompressible smoothed particle hydrodynamics for free-surface flows: A generalised diffusion-based algorithm for stability and validations for impulsive flows and propagating waves. *Journal of Computational Physics*, 231(4):1499–1523, 2012.

[19] Xiaoxing Liu, Koji Morita, and Shuai Zhang. A conservative finite volume-particle hybrid method for simulation of incompressible interfacial flow. *Computer Methods in Applied Mechanics and Engineering*, 355:840–859, 2019. ISSN 0045-7825. doi: 10.1016/j.cma.2019.06.035.

[20] RC Lock and BR Williams. Viscous-inviscid interactions in external aerodynamics. *Progress in Aerospace Sciences*, 24(2):51–171, 1987.

[21] P. Lubin and S. Glockner. Numerical simulations of three-dimensional plunging breaking waves: generation and evolution of aerated vortex filaments. *Journal of Fluid Mechanics*, 767:364–393, 3 2015. ISSN 1469-7645. doi: 10.1017/jfm.2015.62. URL http://journals.cambridge.org/article_S0022112015000622.

[22] Francesca Magionesi, Giulio Dubbioso, Roberto Muscari, and Andrea Di Mascio. Modal analysis of the wake past a marine propeller. *Journal of Fluid Mechanics*, 855:469–502, 2018.

[23] S. Marrone, A. Colagrossi, A. Di Mascio, and D. Le Touzé. Analysis of free-surface flows through energy considerations: Single-phase versus two-phase modeling. *Phys. Rev. E*, 93:053113, May 2016. doi: 10.1103/PhysRevE.93.053113. URL http://link.aps.org/doi/10.1103/PhysRevE.93.053113.

[24] S Marrone, A Colagrossi, L Chiron, M De Leffe, and David Le Touzé. High-speed water impacts of flat plates in different ditching configuration through a riemann-ale sph model. *Journal of Hydrodynamics*, 30(1):38–48, 2018.

[25] Salvatore Marrone, Andrea Colagrossi, David Le Touzé, and Giorgio Graziani. Fast free-surface detection and level-set function definition in SPH solvers. *Journal of Computational Physics*, 229(10):3652–3663, 2010.

[26] Salvatore Marrone, A Di Mascio, and David Le Touzé. Coupling of Smoothed Particle Hydrodynamics with Finite Volume method for free-surface flows. *Journal of Computational Physics*, 310:161–180, 2016.

[27] J. Monaghan and R. A. Gingold. Shock Simulation by the particle method SPH. *Journal of Computational Physics*, 52(2):374–389, 1983.

[28] Angelo Murrone and Hervé Guillard. A five equation reduced model for compressible two phase flow problems. *Journal of Computational Physics*, 202(2):664–698, 2005.

[29] Roberto Muscari, Giulio Dubbioso, and Andrea Di Mascio. Analysis of the flow field around a rudder in the wake of a simplified marine propeller. *Journal of Fluid Mechanics*, 814:547–569, 2017.

[30] Roberto Muscari, Giulio Dubbioso, and Andrea Di Mascio. Analysis of the flow field around a rudder in the wake of a simplified marine propeller. *Journal of Fluid Mechanics*, 814:547–569, 2017.

[31] Enrico Napoli, Mauro De Marchis, Chiara Gianguzzi, Barbara Milici, and Alessandra Monteleone. A coupled Finite Volume–Smoothed Particle Hydrodynamics method for incompressible flows. *Computer Methods in Applied Mechanics and Engineering*, 310:674–693, 2016.

[32] Francis Noblesse, Dane Hendrix, Lisa Faul, and Jonathan Slutsky. Simple analytical expressions for the height, location, and steepness of a ship bow wave. *Journal of Ship Research*, 50(4):360–370, 2006.

[33] Francis Noblesse, GERard Delhommeau, Michel Guilbaud, Dane Hendrix, and Chi Yang. Simple analytical relations for ship bow waves. *Journal of Fluid Mechanics*, 600:105–132, 2008.

[34] G Oger, S Marrone, D Le Touzé, and M De Leffe. SPH accuracy improvement through the combination of a quasi-Lagrangian shifting transport velocity and consistent ALE formalisms. *Journal of Computational Physics*, 313:76–98, 2016.

[35] Stanley Osher. Riemann solvers, the entropy condition, and difference. *SIAM Journal on Numerical Analysis*, 21(2):217–235, 1984.

[36] Anatoly N Parshikov and Stanislav A Medin. Smoothed particle hydrodynamics using interparticle contact algorithms. *Journal of computational physics*, 180(1):358–382, 2002.

[37] Patrick J Roache. Quantification of uncertainty in computational fluid dynamics. *Annual review of fluid Mechanics*, 29(1):123–160, 1997.

[38] PN Sun, Andrea Colagrossi, Salvatore Marrone, Matteo Antuono, and AM Zhang. Multi-resolution delta-plus-sph with tensile instability control: Towards high reynolds number flows. *Computer Physics Communications*, 224:63–80, 2018.

[39] Eleuterio F Toro. *Riemann solvers and numerical methods for fluid dynamics: a practical introduction*. Springer Science & Business Media, 2013.

[40] Renato Vacondio, Corrado Altomare, Matthieu De Leffe, Xiangyu Hu, David Le Touzé, Steven Lind, Jean-Christophe Marongiu, Salvatore Marrone, Benedict D Rogers, and Antonio Souto-Iglesias. Grand challenges for Smoothed Particle Hydrodynamics numerical schemes. *Computational Particle Mechanics*, pages 1–14, 2020.

[41] Bram Van Leer. Towards the ultimate conservative difference scheme. V. A second-order sequel to Godunov's method. *Journal of computational Physics*,

32(1):101–136, 1979.

[42] Stefano Zaghi, Andrea Di Mascio, Riccardo Broglia, and Roberto Muscari. Application of dynamic overlapping grids to the simulation of the flow around a fully-appended submarine. *Mathematics and Computers in Simulation*, 116: 75–88, 2015.